Chemical Engineering Journal 310 (2017) 368–380

Contents lists available at ScienceDirect

Chemical Engineering Journal

journal homepage: www.elsevier.com/locate/cej

# Comprehensive multiphysics modeling of photocatalytic processes by computational fluid dynamics based on intrinsic kinetic parameters determined in a differential photoreactor

Cintia Casado, Javier Marugán *, Ruud Timmers, Marcos Muñoz, Rafael van Grieken

*Department of Chemical and Environmental Technology, ESCET, Universidad Rey Juan Carlos, C/Tulipán s/n, 28933 Móstoles, Madrid, Spain*

## HIGHLIGHTS

- Intrinsic kinetic parameters determined in an optically differential photoreactor.
- Predictive multiphysics CFD simulation of an annular photocatalytic reactor.
- Good correlation between experimental and simulation results for velocity field.
- Optimal $TiO_2$ concentration calculated by radiation absorption simulation.
- Successful experimental validation of CFD conversion predictions with error <10%.

## GRAPHICAL ABSTRACT

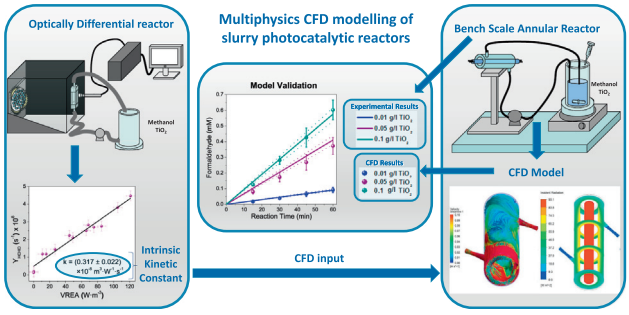


## ARTICLE INFO

*Article history:*
Available online 22 July 2016

*Keywords:*
Photocatalytic reactor
CFD modeling
Validation
Differential
Intrinsic kinetics
Water treatment

## ABSTRACT

This work describes the procedure for the simulation of the operation of a photocatalytic reactor by using a multiphysics computational fluid dynamics (CFD) model based on the determination of the intrinsic kinetics parameters in an optically differential photoreactor. The model includes the rigorous description of the hydrodynamics, radiation transfer, mass transport and chemical reaction rate based on a mechanistic kinetic model. Possible existence of dead and recirculation zones has been identified from the flow field, showing a non-uniform flow through the reactor domain. The theoretical laminar profile is not reached due to the short length of the annular core and the departure from the ideal models has been quantified. The predicted velocity field has been experimentally validated with good agreement by injecting a tracer. The radiation field was simulated for slurry $TiO_2$ suspensions with concentrations between 0.005 and 5 $g{\cdot}L^{-1}$, showing an optimum catalyst loading around 0.1–0.2 $g{\cdot}L^{-1}$. Above this value, the increase in the absorption of radiation is negligible, whereas a more non-uniform radiation profile develops, keeping the most external regions of the reactor in the dark. The results of photocatalytic activity, using methanol oxidation as test reaction, showed good agreement between model predictions and experimental data, with errors between 2% and 10% depending on the catalyst concentration. The successful validation confirms not only the scientific background of the model, but also supports its applicability for engineering purposes in the design and optimization of large scale photocatalytic reactor to overcome some of limitations hindering the industrial development of this technology.



* Corresponding author.
*E-mail address:* javier.marugan@urjc.es (J. Marugán).

http://dx.doi.org/10.1016/j.cej.2016.07.081
1385-8947/

**Nomenclature**

| | |
|---|---|
| ALSPR | annular laboratory scale photoreactor |
| $a_v$ | catalyst surface area per unit volume ($m^{-1}$) |
| $C_{cat}$ | catalyst loading ($g{\cdot}m^{-3}$) |
| CFD | computational fluid dynamics |
| $D_{i,m}$ | diffusion coefficient of species $i$ in the mixture ($m^2{\cdot}s^{-1}$) |
| DOM | discrete ordinate method |
| $\vec{g}$ | gravitational acceleration ($m\ s^{-2}$) |
| $g$ | asymmetry factor of the Henyey-Greentein's phase function (dimensionless) |
| $I$ | radiation intensity (Einstein $m^{-2}\ s^{-1}\ sr^{-1}$) |
| $J_i$ | diffusive flux species $i$ ($kg\ m^{-2}\ s^{-1}$) |
| $k$ | kinetic constant ($m^3\ kmol^{-1}\ s^{-1}$) |
| $p$ | Henyey-Greentein scattering phase function (dimensionless) |
| $P$ | pressure ($N\ m^{-2}$) |
| ODPR | optically differential photoreactor |
| $R_i$ | mass rate of production/depletion of species $i$ ($kg\ m^{-2}\ s^{-1}$) |
| $r_i$ | rate of production/depletion of species $i$ ($kmol\ m^{-3}\ s^{-1}$) |
| RT | residence time (s) |
| RTD | residence time distribution |
| RTE | radiative transfer equation |
| $S_g$ | $TiO_2$ specific surface area of the catalyst ($m^2\ kg^{-1}$) |
| ST | space time ($s^{-1}$) |
| $t$ | time |
| $\bar{v}$ | velocity vector ($m\ s^{-1}$) |
| $V_R$ | reactor volume ($m^3$) |
| $V_T$ | total liquid volume ($m^3$) |
| VREA, $e^a$ | volumetric rate of energy absorption ($W\ m^{-3}$) |
| $Y_i$ | mass fraction of species $i$ in the mixture (dimensionless) |

*Greek letters*

| | |
|---|---|
| $\alpha$ | kinetic parameter ($kmol\ W^{-1}\ s^{-1}$) |
| $\alpha_1$ | kinetic parameter ($kmol\ m^{-3}\ s^{-1}$) |
| $\alpha_2$ | kinetic parameter ($m^3\ W^{-1}$) |
| $\alpha_3$ | kinetic parameter (dimensionless) |
| $\beta$ | volumetric extinction coefficient ($m^{-1}$) |
| $\kappa$ | volumetric absorption coefficient ($m^{-1}$) |
| $\lambda$ | wavelength (nm) |
| $\rho$ | density ($kg\ m^{-3}$) |
| $\sigma$ | volumetric scattering coefficient ($m^{-1}$) |
| $\tau$ | optical thickness (dimensionless) |
| $\bar{\bar{\tau}}$ | stress tensor ($N\ m^{-2}$) |
| $\bar{\Phi}$ | wavelength averaged primary quantum yield ($mol\ Einstein^{-1}$) |
| $\Omega$ | solid angle of radiation propagation about the direction $\underline{\Omega}$ (sr) |
| $\underline{\Omega}$ | unit vector in the direction of radiation propagation |

*Subscripts*

| | |
|---|---|
| HCHO | relative to formaldehyde |
| $i$ | relative to species $i$ |
| $i\_out$ | relative to species $i$ at the reactor inlet |
| $i\_in$ | relative to species $i$ at the reactor inlet |
| Tank | relative to reservoir tank |
| $V_R$ | relative to reactor volume |
| $\lambda$ | indicates dependence on wavelength |
| $\underline{\Omega}$ | indicates a directional dependence |

*Superscripts*

| | |
|---|---|
| s | relative to the reaction rate per unit surface area |

*Special symbols*

| | |
|---|---|
| – | indicates a vectorial magnitude |
| $\langle\rangle$ | indicates average value |

## 1. Introduction

Despite the many advantages of photocatalysis for water purification [1,2] and the extensive laboratory research done in this field, including 13,500 papers, reviews and reference work over the last 38 years [3], photocatalytic technologies for water remediation are not fully industrially developed yet. Tremendous efforts have been devoted to improve photocatalytic efficiency of $TiO_2$ by doping with metals or non-metals or to the development on new photocatalytic materials. Materials improvement has been accompanied with extensive research to identify reaction mechanisms and obtain appropriate kinetic models, but there are several challenges preventing the development of this technology to the commercial scale [1]: mass transfer limitations, catalyst deactivation, generation of intermediate products and by-products and especially low quantum efficiency requiring materials, reactor and light source optimization [2,4,5]. For this purpose, computational fluid dynamics has been shown to be a very promising tool in the design, optimization, and scaling-up of photocatalytic systems for different applications [4–7], saving time, costs and efforts.

Annular reactors have been widely investigated in CFD modeling, as they are the most popular slurry reactors because of the advantageous basic features of this geometry [7,8]. Previous investigations have reported modeling related to hydrodynamics and mass transfer [8–12], irradiance [13,14], and chemical reactions [15–17]. Some studies have also reported the scaling-up of processes to bench scale based on the kinetic constants determined under controlled conditions at lab scale [18,19]. Validation of model predictions with experimental data has been also reported. Passalía et al. [18] determined kinetic parameters experimentally in a lab scale flat plate $TiO_2$ coated reactor (25.6 $cm^3$), under kinetic control regime, and used them in the model of a bench scale corrugated plate type coated with $TiO_2$ as catalyst (1800 $cm^3$) in the gas phase (HCHO as model for indoor pollution control). Also, Elyasi et al. [19] applied the photoreaction rate of the homogeneous UV/$H_2O_2$ degradation of rhodamine WT measured in a bench-scale photoreactor under controlled conditions for the model of a pilot scale photoreactor. Similar methodological approaches have also been reported for immobilized $TiO_2$ [1,15,20].

Rigorous kinetic description of the photocatalytic process requires the explicit inclusion in the model of the photon absorption rate. However, due to the intrinsic nature of photoactivated processes, it is not possible to achieve a uniform light intensity along the whole reactor volume. Therefore, an appropriate knowledge of the irradiance distribution inside the reactor is required through the rigorous resolution of the Radiative Transfer Equation (RTE). Resolution of the RTE in homogeneous systems such as UV/$H_2O_2$ reactors is relatively simple, as scattering of radiation can be neglected and only absorption should be considered. On the other hand, calculation of radiant fluxes in immobilized $TiO_2$ surfaces is also relatively easy to accomplish, as the gas or liquid filling the reactor can be considered usually as non-absorbing media, concentrating radiation absorption on the thin $TiO_2$ layer. In contrast, modeling of the radiation transport in heterogeneous media such

as $TiO_2$ suspensions is mathematically very complex due to the simultaneous presence of volumetric absorption and scattering phenomena.

Determination of intrinsic kinetic parameters in slurry $TiO_2$ reactors is also hindered by the difficulties in the estimation of the Volumetric Rate of Energy Absorption (VREA) in heterogeneous media. Similarly to thermally activated chemical processes, kinetic experiments in photocatalytic systems require working under chemical reaction kinetic control avoiding mass transfer profiles and differential conversions to simplify the mass balances. However, heterogeneous photoactivated processes also require working under optically differential conditions avoiding radiation profiles. Under these conditions, constant concentration of reactants and VREA along the reactor volume can be assumed for the determination of intrinsic (not averaged) kinetic constants. According to Motegh et al. [21] the photocatalytic reactor operates in an optically differential mode when the small gradients in the photon absorption rate do not affect the volume-averaged reaction rate by more than 5%. The suggested maximum optical thickness ($\tau$, product of the extinction coefficient, $\beta$, and the optical path) value was $\tau \approx 0.25$.

The present work reports a procedure for the global modeling of photocatalytic reactors considering all the phenomena involved in the process: i) fluid mechanics, ii) radiation transfer, iii) mass transport, and iv) chemical reaction. The most innovative aspects are related to the coupling in the CFD model of the volumetric chemical reaction rate equation based on intrinsic kinetic parameters with the rigorous resolution of the RTE to determine the local values of the VREA in absorbing and scattering media. To the best of the authors' knowledge, this is the first time that this global approach for the comprehensive multiphysics modeling and simulation of a heterogeneous photocatalytic reactor using $TiO_2$ in suspension and intrinsic kinetic parameters determined in an optically differential photoreactor is reported.

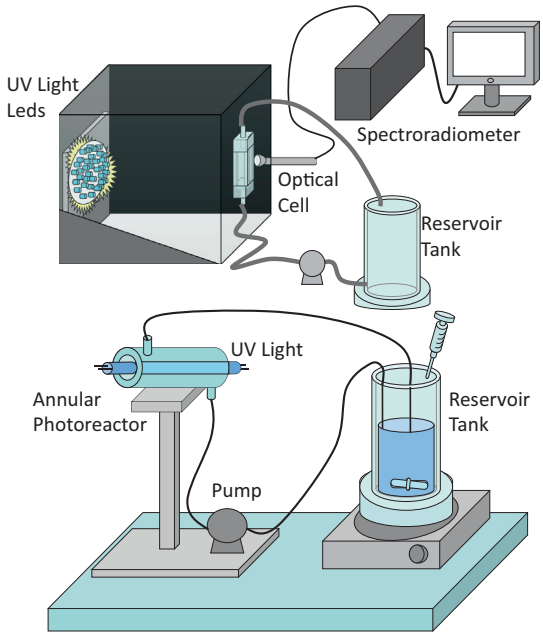


**Fig. 1.** Scheme of the photocatalytic reactors: optically differential photoreactor (ODPR, top), and annular laboratory scale photoreactor (ALSPR, bottom).

## 2. Experimental methods

### 2.1. Photocatalytic reactors

Two different slurry photocatalytic reactors were used: i) an optically differential photoreactor (ODPR) working under optical density conditions low enough to neglect radiation profiles and assume that the radiation intensity is homogeneous throughout its volume in order to get intrinsic kinetic parameters of the photocatalytic process; and ii) an annular laboratory scale photoreactor (ALSPR) working under high optical density conditions to maximize photocatalytic reaction rates. Fig. 1 schematizes both photoreactors.

The ODPR is a 3.2 mL volume continuous flow quartz cell (Hellma QS-130) with an optical path of 1 cm, working under recirculation with a reservoir of 15 mL at a flow rate of 3.25 $mL \cdot min^{-1}$ using a micropump (RS M100S). As irradiation source, a board with 36 UV-A LEDs (LED Engin LZ1-00U600, peak emission at 365 nm, minimum radiant flux of 410 mW at 700 mA), was placed at a distance optimized to achieve a uniform irradiation of the cell. Radiation transmitted through the cell was monitored in continuous mode with a spectroradiometer (BlueWave StellarNet Inc.) located in the central position of the outer side of cell wall. The system is enclosed in a black box to avoid interferences by uncontrolled illumination of the system.

The ALSPR is an annular photoreactor with 50 mm outer tube diameter, 30 mm inner tube diameter, 150 mm total length and 6 mm inlet and outlet diameter tubes, angled 45 degrees to the main reactor body. The illuminated volume is 188.5 $cm^3$. The system operates in a closed recirculating circuit with a well-stirred reservoir tank (1 L total working volume) driven by a centrifugal pump with a flow rate of 2.5 L $min^{-1}$. The UV illumination is provided by a Philips TL 6 W black light fluorescent lamp, 16 mm diameter, 210 mm length, with a maximum emission at 365–370 nm. The lamp is placed in the axis of the annulus.

### 2.2. Materials

Evonik P25 $TiO_2$ was used as photocatalytic material in all the experiments. This material has been widely used in the literature as reference photocatalyst and its optical properties are well known [22]. Methanol (Sigma-Aldrich, LC-MS) at an initial concentration of 100 mM was used as model solution in all photocatalytic tests. All solutions were done in Milli-Q® water (18.2 MΩ·cm).

### 2.3. Reaction procedure

Calculation of the intrinsic kinetic parameters in the ODPR was carried out using catalyst concentrations low enough to meet the criterion for optically differential operation reported by Motegh et al. [21]. Incident light flux and catalyst loading were varied to get experimental data in a wide range of VREA values (0–120 $W \cdot m^{-3}$). UV radiation absorption was measured for each reaction as the difference between the radiant flux transmitted through the cell with the titanium dioxide suspension and that corresponding to pure water, ensuring in all cases that the difference was less than 5% of the latter. This value divided by the optical path (1 cm) provides the estimated average VREA of each reaction under the assumption of negligible back-scattering. The optically differential operation ensures that this average value represents accurately the behavior of the whole ODPR volume. Validation experiments in the ALSPR were carried out at a $TiO_2$ concentration range from 0.01 to 0.1 $g \cdot L^{-1}$ of $TiO_2$ and the fixed UV flux value provided by the lamp.

Preliminary experiments with $TiO_2$ suspensions loaded into the system with the UV source emission and recirculation pump

turned on showed that 30–60 min were required to achieve stabilization of radiation transmission through the cell. This time is required to avoid the effect of $TiO_2$ particles aggregation on the optical properties and ensure a constant VREA during the irradiation time used in the reaction. Agglomeration of the particles has a large impact on the absorption, especially for the very low catalyst concentrations employed in the ODPR. Large agglomerates catch much less light, as more particles are in the shadow inside the agglomerate, and for a given material, the extinction coefficient ($\beta$) scales with the inverse of particle size [21,22]. Consequently, reacting suspensions 100 mM in methanol were recirculated in the dark for 60 min before the irradiation starts. Radiation was continuously monitored during the reaction to ensure constant irradiation conditions.

All reactions lasted 1 h, with samples taken every 15 min ensuring that the total volume extracted from the system does not exceed 10% of the total volume. Aeration and stirring are provided in both reservoirs tanks to ensure good mixing and a constant concentration of dissolved oxygen above 90% of the saturation limit at room temperature. Sampling was undertaken from the reservoir tanks and filtered with 0.22 nm nylon syringe filters to remove $TiO_2$. The progress of the reaction was quantified following the formation of formaldehyde, quantitative oxidation product when methanol is in excess [23]. For analyzing the formaldehyde concentration, the Hantzsh synthesis [24] reaction is used, in which formaldehyde is transformed to 1,4-dihydro-3,5 lutidine diacetyl (DDL), yellowish, that can be monitored by UV/vis. For the ODPR samples, 0.3 mL of buffer solution (0.18 M ammonium phosphate buffer, adjusted to pH 6 with ammonia), 0.3 mL of the sample and 30 μL of acetylacetone are mixed in a test tube. After stirring, the tube is kept in darkness for one hour at ambient temperature before determining the absorbance at 412 nm using a UV/vis spectrophotometer (Biochrom Libra S22). Higher volumes were used for the formaldehyde analysis in ALSPR experiments: 1.5 mL of phosphate buffer, 1.5 mL of sample, 30 μl of acetylacetone. The concentration of formaldehyde produced is calculated with a calibration curve with the same reactant volumes (in both cases $R^2 > 0.99$).

### 2.4. Residence time distribution (RTD)

The RTD is characteristic of the flow pattern inside the vessel volume, being one of the most informative characterization of a chemical reactor [25,26]. For CFD hydrodynamic validation, the RTD of the ALSPR was determined experimentally by using a tracer-response technique. Starting from the system working under stationary circulation of water, methylene blue (Scharlab, extra pure) was injected into the reservoir with a vigorous stirring to assumed a perfect mixture in the vessel at time t = 0. The absorbance at 660 nm in the reactor outlet was monitored in continuous mode with an illuminated flow cell coupled to the spectroradiometer probe. Normalized concentrations were calculated between the baseline at t = 0 and the final absorbance. Fig. 2 shows the scheme of the experimental setup.

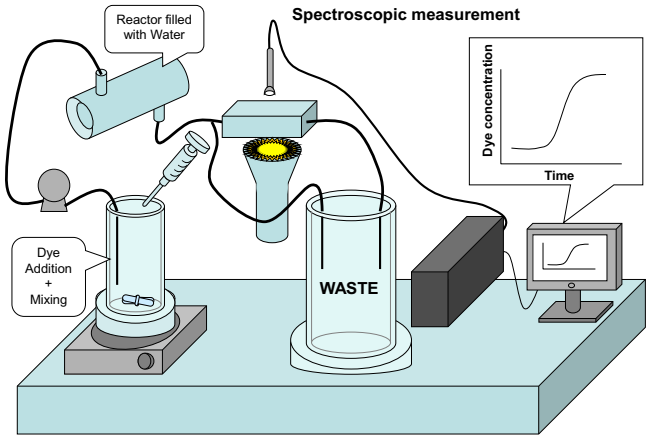


**Fig. 2.** Scheme of the tracer-response setup for the experimental hydrodynamic validation.

## 3. CFD model

### 3.1. Geometry and mesh of the photoreactor

The CFD model has been developed using the commercial software Ansys 14.5 (Ansys Inc.). The ALSPR has been defined to meet the dimensions and characteristics of the experimental system using the Ansys Workbench tool (Fig. 3). The inlet and outlet angles of inclination (to promote mixing), have been carefully included in the model as they have a great impact on the flow field. The lamp was simulated as an empty cylinder defining only the external wall of the lamp. An air domain was defined between the lamp and the reactor to allow the calculation of the radiation transport. The annular reactor volume was discretized in approximately 800000 structured and unstructured volume cells using Ansys Meshing tool. This number of cells has been found to be high enough to give mesh-independent results, corresponding to a mean cell volume of 0.33 $mm^3$. A denser mesh was defined at the inlet and exit sections of the reactor where whirl may occur and large velocity gradients can be present.

### 3.2. Hydrodynamics and mass transfer

The flow field characterization is a very important step to calculate the catalyst distribution in the slurry reactor where non-uniform zones can be present. The simulation of the ALSPR was performed considering a three dimensional, steady state, laminar flow. Hydrodynamics calculations have been carried out assuming a pseudo-homogeneous behavior by means of the resolution of the continuity equation (Eq. (1)) and the classical Navier-Stokes equation (Eq. (2)):

$$\nabla(\rho\bar{v}) = 0 \tag{1}$$

$$\nabla\cdot(\rho\bar{v}\bar{v}) = -\nabla P + \nabla\cdot\bar{\bar{\tau}} + \rho\vec{g} \tag{2}$$

where $\rho$, $\bar{v}$, $P$, $\bar{\bar{\tau}}$ and $\vec{g}$ are fluid density, velocity vector, pressure, viscous stress tensor and gravitational acceleration, respectively. These equations, combined with the Newton's law of viscosity as a constitutive equation to relate the stress tensor to the motion of the continuous fluid, allow computing the velocity field within the reactor. An analytical solution of the system of partial nonlinear differential equations is not available for complex geometries, being solved numerically using a finite volume method based on the discretization scheme described above. The fluids were assumed to be Newtonian, incompressible, and isothermal, with constant physical properties. The inlet velocity was set 1.54 $m\cdot s^{-1}$ (2.5 $L\cdot min^{-1}$) and normal to the boundary. At the outlet, atmospheric pressure was applied. A no-slip boundary condition was imposed at all reactor walls. To calculate the residence time distribution and the validation of the velocity field, the transport of a tracer was simulated (Methylene blue, 0.5 mM, diffusion coefficient $D_{i,m} = 6\cdot10^{-10}$ $m^2\cdot s^{-1}$ [27]) over the steady-state laminar velocity field.

For each individual chemical $i$ in the computational domain, the mass conservation equation can be expressed as:

$$\frac{\partial}{\partial t}(\rho Y_i) + \nabla(\rho\bar{v}Y_i) = \nabla J_i + R_i \tag{3}$$

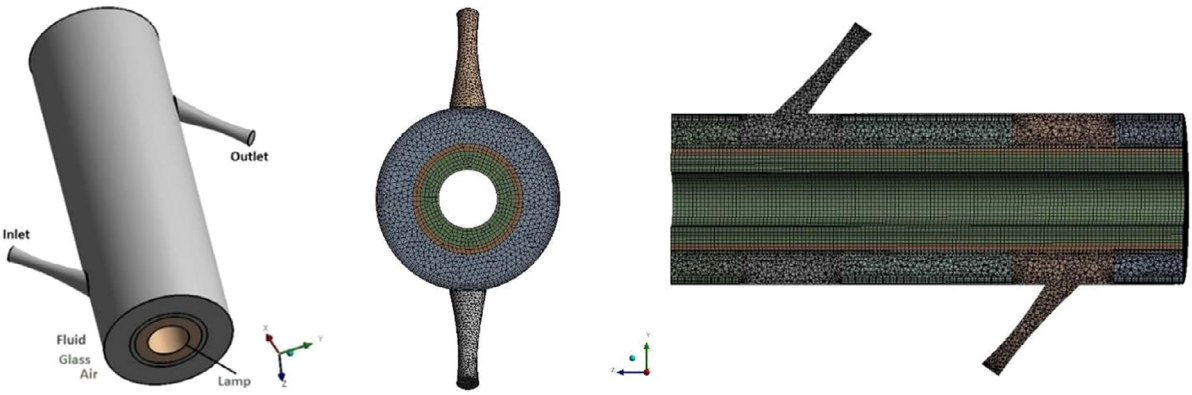


**Fig. 3.** Definition of the ALSPR geometry and discretization mesh.

where $Y_i$ is the fraction of $i$ in the mixture, $J_i$ is its diffusive flux and $R_i$ its rate of production. The velocity vector, $\bar{v}$, couples the mass balances to the hydrodynamics calculations. The diffusive flux can be estimated using Fick's first law of diffusion (Eq. (4)):

$$J_i = -\rho D_{i,m} \nabla Y_i \tag{4}$$

Flow validation in the ALSPR was carried out by comparing the experimental data with the predictions of a non-steady state simulation performed for 50 s with a time step of 0.1 s.

### 3.3. Radiation model

The modeling of photocatalytic reactors requires the resolution of the radiative transfer equation (RTE). This integro-differential equation describes the traveling of photonic rays with their corresponding energy loss due to absorption and out-scattering and energy gain due to in-scattering of photons. Considering the catalyst suspension of a photocatalytic slurry reactor as a pseudo-homogeneous medium, and assuming that the emission of radiation can be neglected at the low operation temperatures of photocatalytic processes, the RTE takes the following form [28]:

$$\frac{dI_{\lambda,\underline{\Omega}}}{ds} = -\kappa_\lambda I_{\lambda,\underline{\Omega}} - \sigma_\lambda I_{\lambda,\underline{\Omega}} + \frac{\sigma_\lambda}{4\pi} \int_{\Omega'=4\pi} p(\underline{\Omega}' \rightarrow \underline{\Omega}) I_{\lambda,\underline{\Omega}'} d\Omega' \tag{5}$$

where $I_{\lambda,\underline{\Omega}}$ is the intensity of photons with wavelength $\lambda$ propagated along direction $\underline{\Omega}$, $\kappa_\lambda$ is the volumetric absorption coefficient, $\sigma_\lambda$ is the volumetric scattering coefficient and $p(\underline{\Omega}' \rightarrow \underline{\Omega})$ is the phase function that describes the directional distribution of scattered radiation. The solution of this equation allows the evaluation of the radiation field at any point inside the reactor space. Once the intensities are known, the incident radiation can be readily obtained and the local VREA can be calculated multiplying this value by the absorption coefficient. Numerical resolution of the RTE was carried out using the Discrete Ordinate Method (DOM). This method solves the RTE for a finite number of discrete solid angles, each one associated with a vector direction. When using the DOM, the spatial discretization of the computational region is taken directly from the mesh grid topology. However, the directional discretization for the RTE was explicitly specified using an angular discretization of the sphere octant of $10 \times 10$ divisions (enough to avoid the well-known "ray effect") and $3 \times 3$ pixelation (enough to overcome angle overhanging).

The scattering and absorption coefficients together with the phase function parameter are optical properties that play an important role in the overall design of a photoreactor. Since solving the RTE for each individual wavelength can be computationally very expensive, the UV-A spectral band between 340 and 400 nm in which the emission spectrum of the lamp and the absorption of the $TiO_2$ catalyst suspension overlap was solved assuming wavelength averaged values of the optical properties of P25 $TiO_2$ aqueous suspensions taken from the literature [22]. The volumetric absorption and scattering coefficients (in $m^{-1}$) were calculated by multiplying the corresponding specific values by the mass loading of catalyst ($C_{cat}$, in $g \cdot m^{-3}$) as follows:

$$\kappa_{365} = 0.867 \times C_{cat} \tag{6}$$

$$\sigma_{365} = 4.655 \times C_{cat} \tag{7}$$

For the calculation of radiation scattering, the Henyey and Greenstein phase function (Eq. (8)) was included in the model as a subprogram (User Defined Function, UDF), using an averaged value of $g_\lambda = 0.528$ also obtained for the literature [22].

$$p_\lambda(\theta) = \frac{1}{4\pi} \frac{(1 - g_\lambda^2)}{(1 + g_\lambda^2 - 2g_\lambda \cos\theta)^{3/2}} \tag{8}$$

Finally, as boundary for the resolution of the RTE, a surface emission model was consider for the light source, as this model has been previously found to be appropriated to represent fluorescent UV lamps [29,30]. The lamp wall was set as semi-transparent purely diffuse wall with a 93.1 $W \cdot m^{-2}$ of external irradiance (calculated dividing the UV-A power output of the lamp by the envelope surface area). All the remaining walls were set as zero-thickness and also semi-transparent. The temperature was fixed to 1 K in all domains to inactivate calculations of radiation emission.

### 3.4. Chemical reaction

The performance of the ALSPR was simulated for different concentration values of $TiO_2$ suspensions between 0.01 and 0.5 $g \cdot L^{-1}$. Photocatalytic oxidation of methanol was chosen as model reaction test. Preliminary experiments confirmed that photolysis without catalysts and dark adsorption effects could be neglected from the kinetic description of the process. The proposed reaction mechanism including explicitly the radiation absorption step, charge transfer and radicals propagation is detailed in Table 1.

The use of methanol in excess leads to a low conversion below 5%, and therefore initial reaction conditions can be assumed for the kinetic analysis. Moreover, under conditions of excess of methanol and presence of oxygen, formaldehyde oxidation to formic acid and eventually $CO_2$ can be neglected, allowing the assumption of quantitative formation of formaldehyde [33] according to the following global stoichiometry:

$$CH_3OH + \frac{1}{2} O_2 \rightarrow HCHO + H_2O$$

**Table 1**
Proposed reaction scheme of the photocatalytic oxidation of methanol based on hydroxyl radical generation.

| Step | Reaction | Rate |
|---|---|---|
| Activation [31,32] | $TiO_2 + h\nu \rightarrow TiO_2 + e^- + h^+$ | $r_g$ |
| Recombination [31,32] | $e^- + h^+ \rightarrow$ heat | $k_2[e^-][h^+]$ |
| Electron trapping [31,32] | $e^- + O_2 \rightarrow \cdot O_2^-$ | $k_3[e^-][O_2]$ |
| Hole trapping [31,32] | $h^+ + H_2O \rightarrow \cdot OH + H^+$ | $k_4[h^+][H_2O]$ |
| Radicals propagation [33,34] | $\cdot OH + CH_3OH \rightarrow H_2O + \cdot CH_2OH$ | $k_5[\cdot OH][CH_3OH]$ |
| [33,34] | $\cdot CH_2OH + O_2 \rightarrow HCHO + HO_2^{\cdot}$ | $k_6[\cdot CH_2OH][O_2]$ |
| [35] | $\cdot OH + HCHO \rightarrow \cdot OCH + H_2O$ | $k_7[\cdot OH][HCHO]$ |
| [35] | $\cdot OH + \cdot OCH \rightarrow HCOOH \rightarrow \ldots \rightarrow CO_2 + H_2O$ | $k_8[\cdot OH][\cdot OCH]$ |

The intrinsic kinetic model of the reaction can be expressed by the following expression (details of the derivation of the kinetic model can be found in Appendix A):

$$r_{HCHO} = \alpha_1 \frac{[CH_3OH]}{[CH_3OH] + \alpha_3[HCHO]} \left(-1 + \sqrt{1 + \alpha_2 e^a}\right) \quad (9)$$

When methanol is in a large excess, $\alpha_3[HCHO] << [CH_3OH]$, Eq. (9) will take the form:

$$r_{HCHO} = \alpha_1 \left(-1 + \sqrt{1 + \alpha_2 e^a}\right) \quad (10)$$

Moreover, for low irradiation conditions, $\alpha_2 e^a << 1$, taken the first term of the square root Taylor expansion, Eq. (10) can be simplified to:

$$r_{HCHO} = \alpha e^a \quad (11)$$

where the formaldehyde production rate ($r_{HCHO}$, kmol·m$^{-3}$·s$^{-1}$) can be reasonably described as proportional to the VREA ($e^a$, W·m$^{-3}$). The kinetic parameter of the process, ($\alpha$, kmol·W$^{-1}$·s$^{-1}$), was experimentally determined under controlled conditions in the ODPR.

Simulation of the batch recirculation regime of the ALSPR operation was conducted in non-steady state with initial mass fractions of methanol and oxygen of $3.2 \times 10^{-3}$ and $9.1 \times 10^{-6}$, corresponding to 0.1 M of $CH_3OH$ and air-saturated water, respectively. The dilution effect that takes place in the reservoir tank was also introduced in the model by a subprogram code (UDF) according to Eq. (10):

$$Y_i = \frac{Y_{i\_out} \cdot \Delta t + \tau \cdot Y_{i\_in}}{\Delta t + ST} \quad (12)$$

where $Y_i$ is the inlet fraction of species every time step, ST is the space time in the reservoir tank (16.6 s) and $\Delta t$ is the time step (1 s).

### 3.5. Convergence criteria and solution strategy

The segregated steady-state solver was used to solve the governing equations. Second order upwind discretization scheme was employed except for pressure for which the standard method was selected. The SIMPLE algorithm was chosen for the pressure–velocity coupling. Convergence of the numerical solution was ensured by monitoring the scaled residuals to a criterion of at least $10^{-6}$ for the continuity, momentum variables and incident radiation, and $10^{-4}$ for the concentrations. Additionally, the variables of interest have been monitored at different surfaces of the computational domain as indicator of convergence (at least 50 iterations without changes). To carry out the simulation the model was solved in three steps: first the flow field (equations of conservation of mass and momentum), then, the radiation field and finally, the conservation of species (including chemical reaction). The fluid flow and the radiation balance were solved in stationary state, then, the photocatalytic reaction was simulated in a transient mode, with a 1 s time step. This strategy can be used when velocity and radiation fields did not interact [30], saving computational time and providing stability to the system.

The computational time required to calculate a complete reaction using a standard personal computer was above 24 h. Future work will focus on approaches to reduce the required computational time, enabling the use of the model with optimization purposes.

## 4. Results and discussion

### 4.1. Hydrodynamics

To predict the behavior of photocatalytic reactors, and especially important for the scaling-up process, it is necessary to determine quantitatively the departure of the real flow in the reactor from the ideal models, and the possible consequences for the functioning of the system. The magnitude of the non-ideality is not controllable in scale changes, which can lead to serious errors in the design. Fig. 4 shows the streamlines of velocity magnitude calculated for the ALSPR assuming a laminar model (Re = 665). It is very clear from the streamlines that the flow is not uniform through the annular region. The 45° inclination angle of the inlet pipe causes that the fluid, which enters at high speed, impacts with the back cover of the reactor, and return to the annular area (backflow regions), due to sudden expansion and change in direction of flow. On the other hand, there is an important dead zone in front of the outlet zone where velocity magnitude is very low.

For a better understanding of flow pattern, velocity vectors have been obtained at different distances from the top of the reactor (Fig. 5). The velocity vectors for the plane located at 1 cm show that flow goes though the inlet side (left side) and impact with the inner tube, splitting the flow. The fluid surrounds the inner tube until reaching half of the annulus, where start going next to the outer wall, causing the collision in front of the inlet tube. A secondary current goes directly to the reactor bottom next to the inlet side. At 5 cm there is a mixing zone where velocity direction is fluctuating. Near the outlet tube, at 10 cm, the flux goes to outlet side with higher velocities and in a more homogeneous way and meets the secondary current that comes from the bottom of the reactor. After the outlet tube (14 cm), fluid goes to the right side to leave the reactor.

The velocity field has been validated through the experimental determination of the residence time distribution (RTD) by injection of a tracer. The numerical RTD was simulated by solving a transient mass transport equation in the reactor domain. Residence Time (RT) and variance value were calculated as reported in [26]. The calculated RT values were 5.6 and versus 4.3 s for the CFD prediction and the experimental RTD, and variance values of 4.2 and 10.6 s$^2$, respectively. This difference may be reasonably attributed to the experimental error associated to the dead pipe volumes of the ALSPR setup. The tanks-in-series model, where the real annular reactor is replaced by a series of consecutive ideal stirred tank reactors, was used to characterize quantitatively the experimental

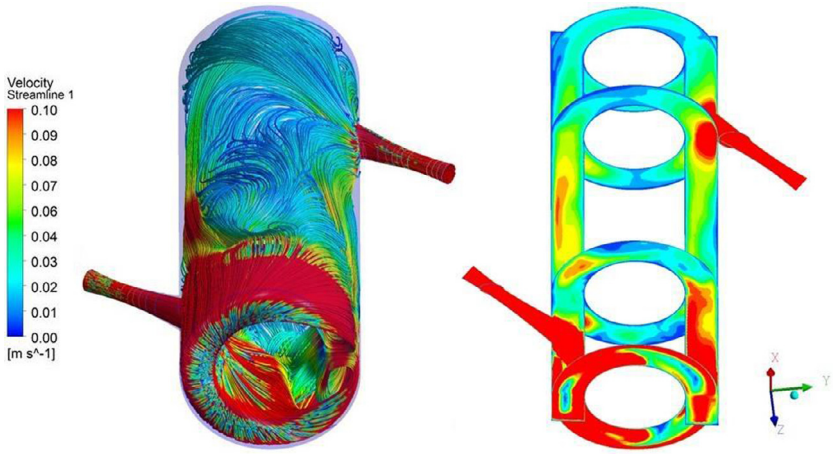


**Fig. 4.** Streamlines (left) and contours of velocity magnitude at different section planes located at 1, 5, 10 and 14 cm positions (right).

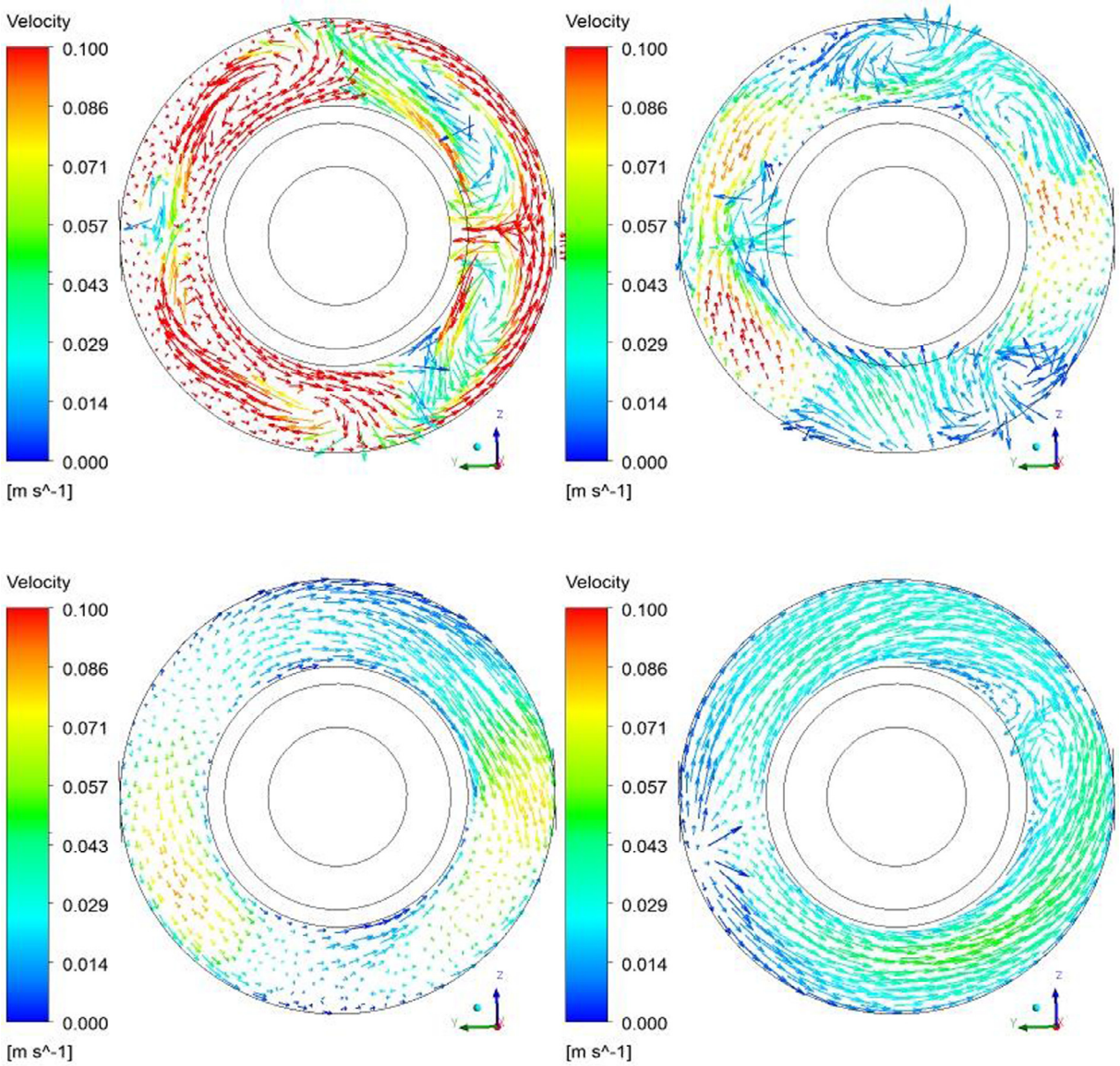


**Fig. 5.** Velocity vectors along the axial plane at different distances from the bottom of the reactor: 1 cm (top left), 5 cm (top right), 10 cm (bottom left) and 14 cm (bottom right).

RTD [25], being estimated a number of 3 reactors. Fig. 6 top shows that a good agreement is found between the RTD estimated by CFD and the theoretical predictions of the 3 tanks-in-series model.

Although the reactor is theoretically operating under laminar flow regime, the short length of the reactor and the turbulence generated at the reactor entrance assure good mixing conditions, as concluded in a previous work [36]. Moreover, the flow is not fully developed through the reactor, unlike most of the flow patterns calculated in other annular photoreactors, in which, at some length, the theoretical profile of laminar flow is reached. This is because annular reactors are usually modeled longer, between the range of 50–90 cm, but similar recirculation zones where showed close to the entrance/outlet regions [8–10]. The theoretical calculation of the fully developed flow inside an annular reactor was calculated without taking into account the inlets sections (Fig. 6 bottom) as reported elsewhere [26]. CFD simulation of reactor lengths of 30 and 45 cm were also carried out to check the impact in the profiles of velocity magnitude along the center plane of the annular region length. The calculated profiles, also displayed in Fig. 6 bottom, clearly confirm the strong non-ideality of the flow inside the reactor volume.

### 4.2. Radiation

The results of the radiation field simulations in the ALSPR for different titanium dioxide concentrations are displayed in Fig. 7. The profiles show how absorption takes place in a narrow strip close to the radiation entrance wall, indicating that irradiance dropped drastically through the fluid. That strip is narrower as the catalyst loading increases, leaving most of the reactor in darkness for a concentration of 0.5 $g \cdot L^{-1}$ of $TiO_2$. Fig. 8 plots the decreasing profile of the VREA along the radial position of the annular region for increasing catalyst concentrations. As it can be noticed, above 0.1 $g \cdot L^{-1}$ profiles cross among them meaning that the most external part of the reactor is absorbing less radiation than for lower catalyst concentration.

The reactor volume averaged value of the VREA ($W \cdot m^{-3}$) calculated from the radiation field in the ALSPR increases with the catalyst concentration, as expected for higher absorption and scattering coefficients, reaching a maximum for a value of 0.2 $g \cdot L^{-1}$ (Fig. 9 top). Above this value, the increase is almost negligible and the total absorbed energy remains approximately constant. This optimum catalyst loading obviously depends on the reactor geometry, lamp emission power and the optical properties of the catalyst, and therefore it cannot be directly extrapolated to a different system. In any case, these results are in good agreement with previous reports involving P25 $TiO_2$ suspensions for the inactivation of bacteria in a different photocatalytic reactor [36]. Moreover, the optical thickness corresponding to the reactor operation at 0.2 $g \cdot L^{-1}$ is 11.0, in good agreement with the optimal values for the operation of photocatalytic reactors estimated by Colina-Marquez et al. using a six-flux radiation model [37].

Fig. 9 (bottom) shows the total energy balance in the ALSPR, experimentally validated with experimental measurements of the outgoing radiation fluxes (not shown). For low catalyst concentrations, backscattering can be neglected, being the losses through the external wall the main energy term. The increase in the catalyst loading leads to an increase in the losses by backscattering, but particularly increases the absorption term. Above 0.2 $g \cdot L^{-1}$ the losses by backscattering decrease, but the small improvement in absorption does not justify the use of a significantly higher amount of catalyst, neither the use of reflecting media in the external wall to recover the losses of radiation.

Radiation scattering has an unexpected effect on the average incident radiation. As shown in Fig. 9 top, the dependence of the incident radiation flux averaged on the reactor volume on the catalyst concentration shows a maximum at a low value around 0.02 g $L^{-1}$. The reason is that for low $TiO_2$ loading, the effect of the scattering inside the reactor volume reduces the losses of radiation through the external wall, increasing the incident radiation in more extent than the decrease due to absorption.

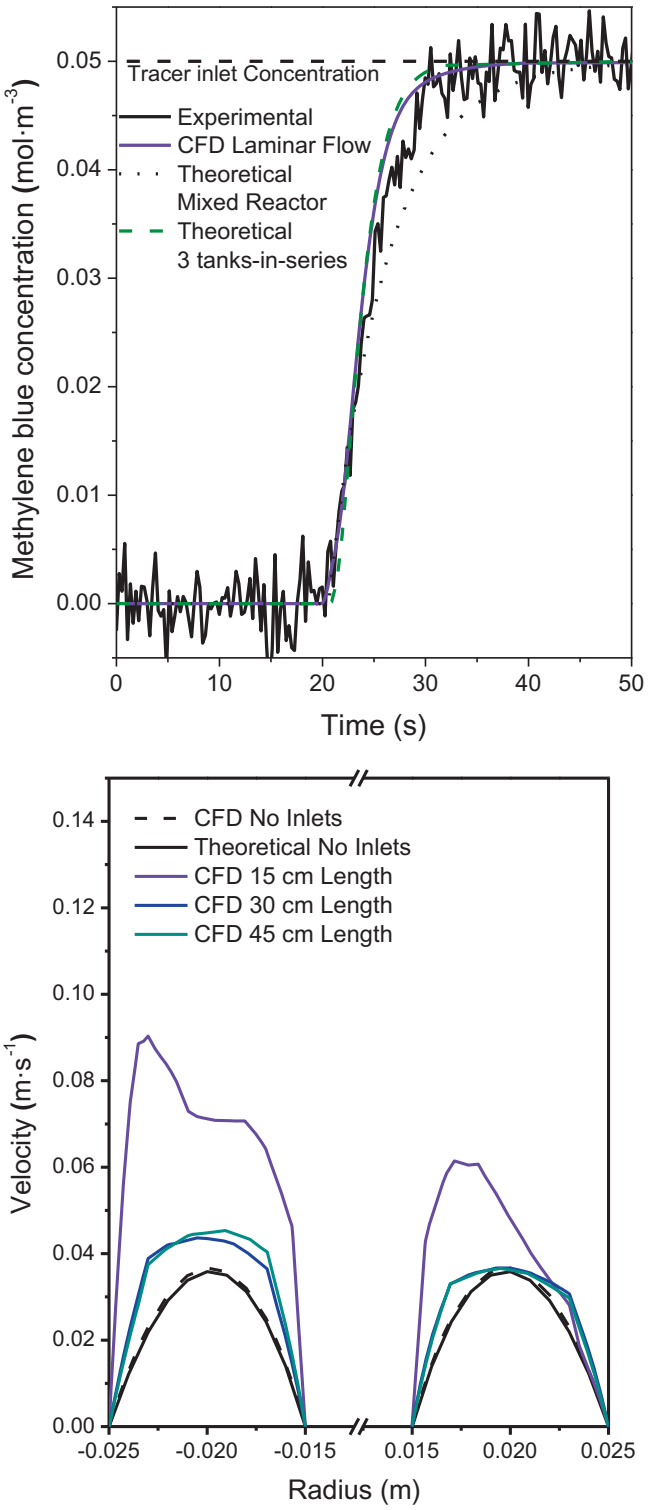


**Fig. 6.** Comparison of experimental vs. CFD residence time distribution (RTD) of the ALSPR (top). Dotted and dashed lines represent the theoretical RTD curves (RT = 4.23 s) for a well-mixed tank reactor and a 3-tanks in series model, respectively. Velocity magnitude profiles along the radial position at the central position of the reactor for different total reactor lengths (bottom).

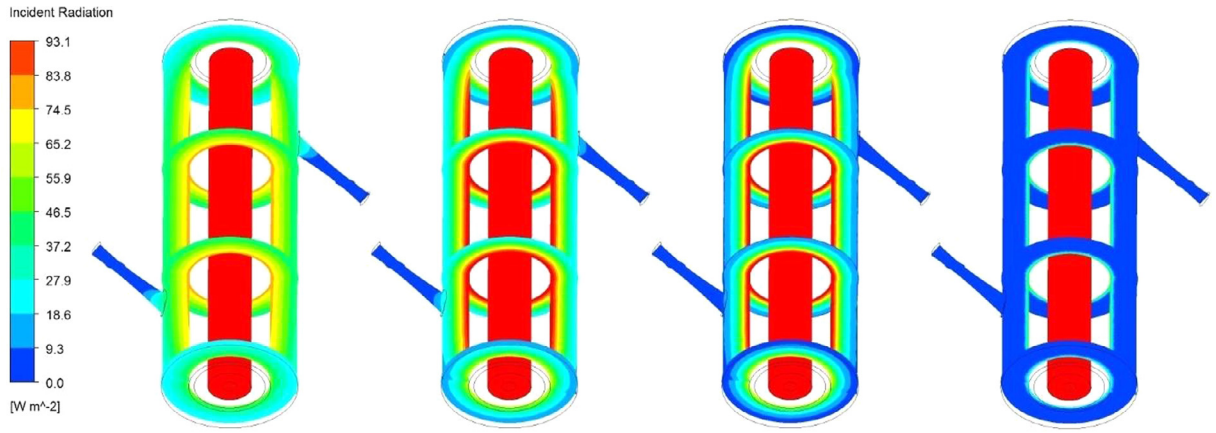


**Fig. 7.** Contours of irradiance distribution for different $TiO_2$ concentrations: 0.01, 0.05, 0.1 and 0.5 g·L$^{-1}$ from left to right, respectively.

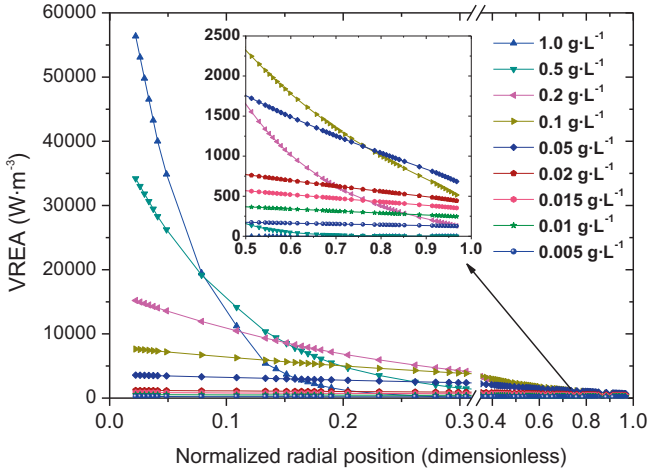


**Fig. 8.** Radial profiles of the VREA in the annular region, calculated at the central position of the reactor length (results are symmetric in all angular directions).

However, above 0.02 g·L$^{-1}$ the absorption effect, together with losses by backscattering, predominates over the recapturing effect of scattering inside the reactor volume, decreasing the incident radiation available at the most external reactor regions.

### 4.3. Photocatalytic activity

The value of the intrinsic kinetic constant required for the simulations was estimated from the experimental data obtained in the ODPR. Assuming that: i) the system is perfectly mixed (ii) there are no mass transport limitations; iii) the conversion per pass in the reactor is differential; and iv) there are no parallel dark reactions, the mass balance of formaldehyde in the reservoir tank of the ODPR (where samples are taken) can be expressed as:

$$\left.\frac{d[\mathrm{HCHO}]}{dt}\right|_{Tank} = \frac{V_R}{V_T}\langle r_{\mathrm{HCHO}}\rangle_{V_R} \tag{13}$$

where the volume-averaged reaction rate can be computed from the volume-averaged term of radiation absorption of the intrinsic kinetic model:

$$\langle r_{HCHO}\rangle_{V_R} = \alpha_1\left(-1+\left\langle\sqrt{1+\alpha_2 e^a}\right\rangle_{V_R}\right) \tag{14}$$

Assuming the optically differential operation of the ODPR, Eq. (14) can be approximated by:

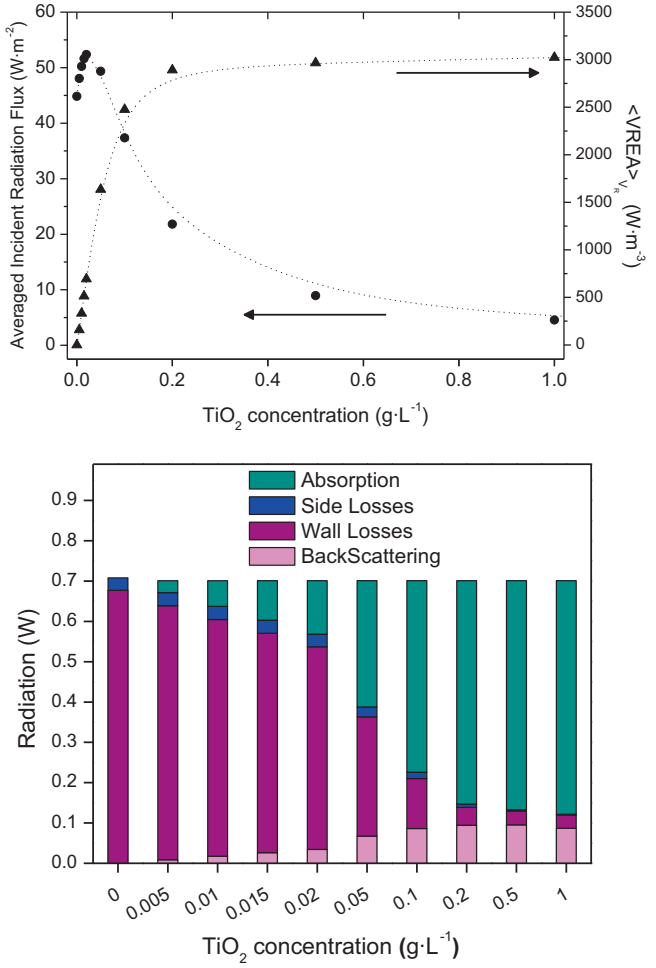


**Fig. 9.** Volume averaged incident radiation and VREA (top) and radiation balance (bottom) as a function of catalyst concentration.

$$\langle r_{HCHO}\rangle_{V_R} = \alpha_1\left(-1+\sqrt{1+\alpha_2\langle e^a\rangle_{V_R}}\right) \tag{15}$$

or the corresponding low irradiation limiting case:

$$\langle r_{HCHO}\rangle_{V_R} = \alpha\langle e^a\rangle_{V_R} \tag{16}$$

where the value of the VREA averaged on the reactor volume is experimentally measured.

Consequently, the value of the intrinsic kinetic parameters can be calculated from the plot of the reaction rate of formaldehyde production versus the VREA averaged in the reactor volume and measured by radiometry in the cell of the ODPR. Fig. 10 represents the fitting of the experimental data to both Eq. (16) ($\alpha = 3.17 \pm 0.22 \times 10^{-10}$ kmol·W$^{-1}$·s$^{-1}$) and Eq. (15) ($\alpha_1 = 5.12 \pm 21.0 \times 10^{-7}$ kmol·m$^{-3}$·s$^{-1}$, $\alpha_2 = 1.13 \pm 5.10 \times 10^{-3}$ m$^3$·W$^{-1}$), where it can be noticed that both models leads to similar fitting. Although the value for $R^2$ of model Eq. (15) is slightly higher, the confidence interval of its kinetics parameters includes the zero value, indicating a strong correlation between both parameters. Moreover, the approximation of the simplified linear model Eq. (16) is supported by the fact that $\alpha_2 e^a << 1$.

Predictions of the ALSPR performance were simulated based on the resolution of the CFD model including the intrinsic kinetics for the chemical reaction in the non-steady state species mass balances. Simulations have been carried out using both kinetic model expressions given by Eq. (10) and Eq. (11). Mass transfer contours follow the same pattern than the velocity distribution (data not shown). The local values of the chemical reaction rate calculated by the UDF using the dependence of the VREA distribution given by Eq. (11) in the whole reaction domain are represented in Fig. 11. The radial profiles of the reaction rate along the middle length plane (7.5 cm) of the annular region shows that a concentration of 0.1 g L$^{-1}$ leads to high reaction rates close to the radiation entrance wall whereas the most external part of the reactor is almost inactive.

Finally, the predicted evolution of formaldehyde concentration on the reservoir tank of the ALSPR can be calculated from the CFD model output. Fig. 12 shows the CFD predictions and the experimental results for the concentration of formaldehyde versus time for three different $TiO_2$ concentrations.

Simulations using the kinetic model given by Eq. (11) show a very good agreement, with less than 5% of error for both 0.10 and 0.01 g·L$^{-1}$ of $TiO_2$. For 0.05 g/L of $TiO_2$, a higher error of 10% is obtained, computed from the difference between the slope of the predicted formaldehyde formation and the fitting of the experimental data. In any case, these values can be considered more than acceptable, as they are in the range of the experimental error.

In contrast, the CFD simulations using the kinetic model given by Eq. (10) fail to predict satisfactorily the performance of the ALSPR. Fig. 13 plots the dependence of the reaction rate on the average VREA estimated for the reactor by solving the RTE. As it can be seen, the ALSPR is operating under much higher values of the VREA that the ODPR, and consequently the kinetic model is being extrapolated. As shown in Fig. 13 the linear dependence

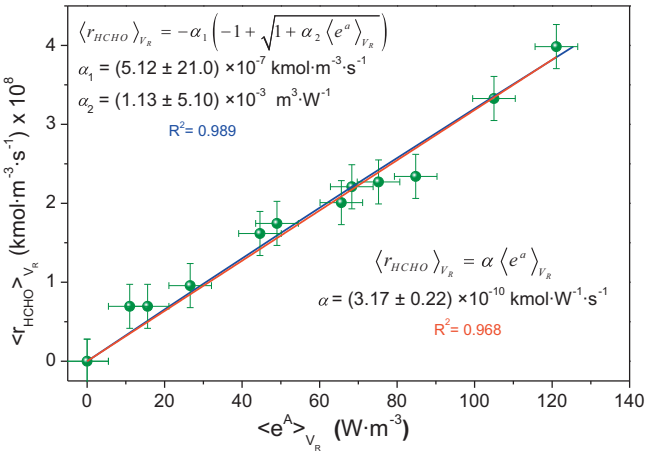


**Fig. 10.** Determination of the intrinsic kinetic parameters based on the ODPR experimental data.

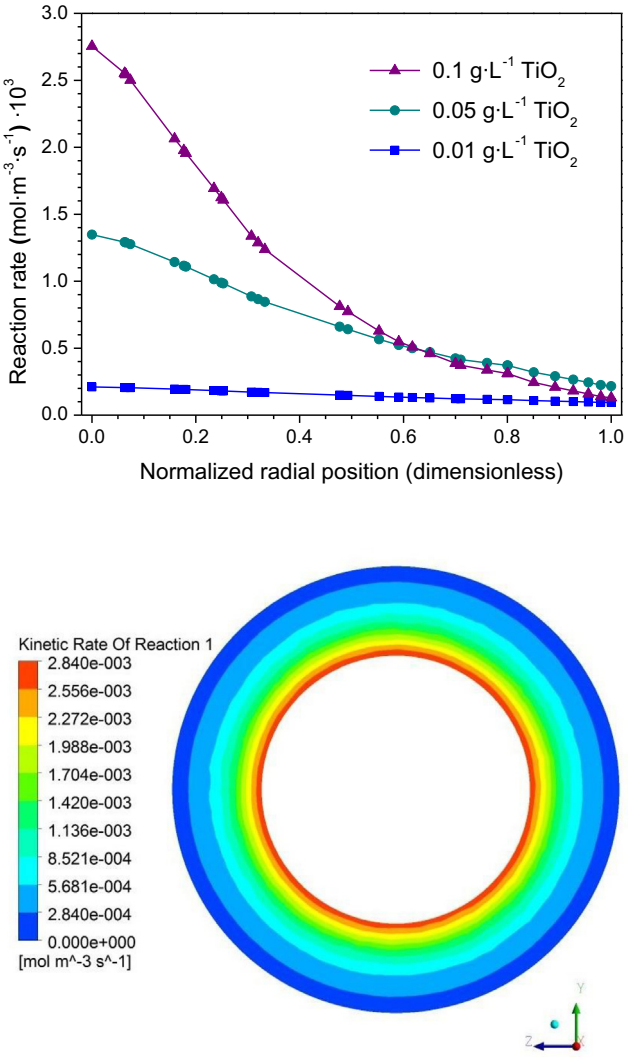


**Fig. 11.** Local values of the chemical reaction rate calculated in the whole reaction domain: Radial profiles along the middle-length plane (7.5 cm) for increasing catalyst concentration (top) and contour plot for 0.1 g·L$^{-1}$ (bottom). All values correspond to an irradiation time of 1800 s.

given by Eq. (11) (in red) leads to a reasonable estimation of the reaction rates. However, the extrapolation of the VREA dependence given by Eq. (10) (in blue) significantly underestimates the kinetics of the process, especially for high values of the average VREA. Fig. 13 also shows the comparison between the predictions of the CFD model based on the rigorous description of the hydrodynamic, radiation transport and mass transfer in the reactor (dots) in comparison with the direct plot of the kinetic expressions Eq. (10) and Eq. (11) (lines). In the case of the complex dependence on the VREA given by Eq. (10), the discrepancies can be attributed both to the non-ideal flow pattern along the reactor and the significant error involved in the approximation of the average VREA for highly non-uniform radiation profiles such as those present in the ALSPR. However, for the linear VREA dependence given by Eq. (11), the discrepancies would be exclusively due to the non-ideal flow in the reactor, being noticed an improvement in the prediction when the CFD model is used. Therefore a very successful validation of the model predictions can be certainly concluded, confirming the usefulness of CFD tools for the rigorous description of photocatalytic reactors.

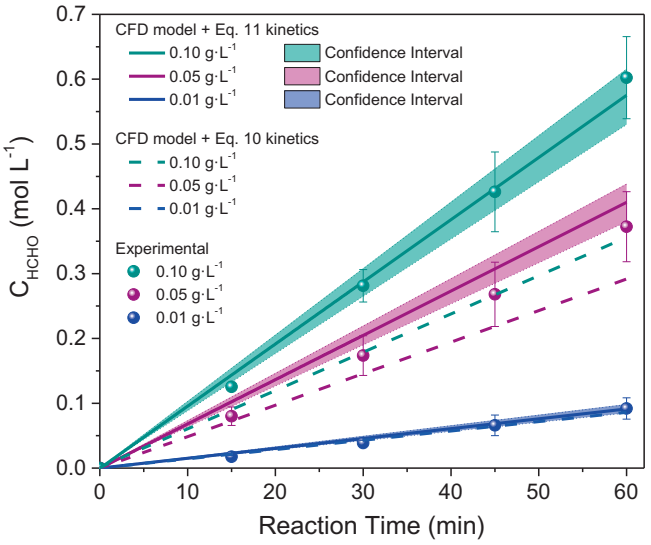


**Fig. 12.** Validation of the CFD simulation results with ALSPR experimental data using different catalyst concentrations.

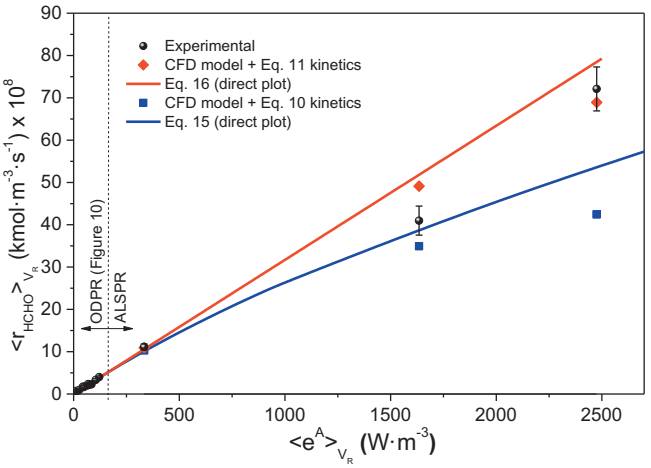


**Fig. 13.** Plot of reaction rate versus averaged VREA for experimental runs in ODPR and ALSPR systems and comparison with CFD simulations and direct plot of the kinetic expressions.

## 5. Conclusions

A comprehensive multiphysics CFD model for the simulation of the photocatalytic reactor was developed, including description velocity field, radiation profile, species transport and volumetric reaction rate. The effect of recirculation and dilution in the reservoir tank in transient regime are also included in the model. Predictive performance of an annular reactor was simulated based on the kinetic parameters experimentally determined in an optically differential photoreactor. The successful validation with experimental data of the model predictions confirms not only the scientific background of the model, but also supports its applicability for engineering purposes in the design and optimization of large scale photocatalytic reactor to overcome some of limitations hindering the industrial development of this technology.

## Acknowledgements

The authors gratefully acknowledge the financial support of the Spanish Ministry of Economy and Competitiveness (MINECO), in the frame of the collaborative international consortium WATER-JPI2013 – MOTREM of the Water Challenges for a Changing World Joint Programming Initiative (Water JPI) Pilot Call. The LED light source has been also partially financed by the European Commission under FP7 project 309846, "Photocatalytic Materials for the Destruction of Recalcitrant Organic Industrial Waste – PCATDES" thanks to a collaboration with the University of Bath. Cintia Casado also acknowledges MINECO for the FPI grant (BES-2012-056661).

## Appendix A. Derivation of the kinetic model

The kinetic model proposed for the photocatalytic oxidation of $CH_3OH$ is based on the reaction scheme summarized in Table 1. By applying the kinetic micro steady state approximation (MSSA) for the concentration of electrons, holes and radicals, the following expressions can be derived:

$$r_{e^-} = \frac{d[e^-]}{dt} = r_g - k_2[e^-][h^+] - k_3[e^-][O_2] \approx 0 \quad (A1)$$

$$[e^-] = \frac{r_g}{k_2[h^+] + k_3[O_2]} \quad (A2)$$

$$r_{h^+} = \frac{d[h^+]}{dt} = r_g - k_2[e^-][h^+] - k_4[h^+][H_2O] \approx 0 \quad (A3)$$

$$[h^+] = \frac{r_g}{k_2[e^-] + k_4[H_2O]} \quad (A4)$$

$$\begin{aligned} r_{\cdot OH} &= \frac{d[\cdot OH]}{dt} \\ &= k_4[h^+][H_2O] - k_5[\cdot OH][CH_3OH] - k_7[\cdot OH][HCHO] \\ &\quad - k_8[\cdot OH][\cdot OCH] \\ &\approx 0 \end{aligned} \quad (A5)$$

$$[\cdot OH] = \frac{k_4[h^+][H_2O]}{k_5[CH_3OH] + k_7[HCHO] + k_8[\cdot OCH]} \quad (A6)$$

$$r_{\cdot CH_2OH} = \frac{d[\cdot CH_2OH]}{dt} = k_5[\cdot OH][CH_3OH] - k_6[\cdot CH_2OH][O_2] \approx 0 \quad (A7)$$

$$[\cdot CH_2OH] = \frac{k_5[\cdot OH][CH_3OH]}{k_6[O_2]} \quad (A8)$$

$$r_{\cdot OCH} = \frac{d[\cdot OCH]}{dt} = k_7[\cdot OH][HCHO] - k_8[\cdot OH][\cdot OCH] \approx 0 \quad (A9)$$

$$[\cdot OCH] = \frac{k_7[\cdot OH][HCHO]}{k_8[\cdot OH]} = \frac{k_7[HCHO]}{k_8} \quad (A10)$$

Introducing Eq. (A2) into Eq. (A4), the expression for the hole concentration is obtained:

$$\begin{aligned} [h^+] &= \frac{r_g}{k_2\frac{r_g}{k_2[h^+]+k_3[O_2]}+k_4[H_2O]} = \frac{r_g\left(k_2[h^+]+k_3[O_2]\right)}{k_2 r_g + k_4[H_2O](k_2[h^+]+k_3[O_2])} \\ [h^+]^2 &+ \frac{k_3[O_2]}{k_2}[h^+] - \frac{r_g k_3[O_2]}{k_4[H_2O]k_2} = 0 \end{aligned} \quad (A11)$$

From the solution of Eq. (11) (the positive root is the only one that has physical meaning) [31,32]:

$$[h^+] = \frac{k_3[O_2]}{2k_2}\left(-1 + \sqrt{1 + \frac{4r_g k_2}{k_3 k_4[H_2O][O_2]}}\right) \quad (A12)$$

Besides, the superficial rate of electron-hole generation is given by [31]:

$$r_g^s(\mathbf{x}) = \frac{\overline{\Phi}}{a_V}\int_\lambda e_\lambda^a(\mathbf{x})d\lambda = \frac{\overline{\Phi}e^a(\mathbf{x})}{S_g C_{cat}} \tag{A13}$$

Considering that the catalyst slurry can be described as a pseudo homogeneous system, the reaction rate of the activation step can be expressed in a volumetric basis as:

$$r_g(\mathbf{x}) = r_g^s(\mathbf{x})a_V = \overline{\Phi}\int_\lambda e_\lambda^a(\mathbf{x})d\lambda = \overline{\Phi}e^a(\mathbf{x}) \tag{A14}$$

where $e^a(\mathbf{x})$ represents the local volumetric rate of photon absorption (LVRPA) and $\overline{\Phi}$ is the primary quantum yield averaged over the wavelength range.

Then, from Eqs. (A6), (A12) and (A14), results:

$$[\cdot OH] = \frac{k_4[H_2O]}{k_5[CH_3OH] + k_7[HCHO] + k_8[\cdot OCH]} \times \frac{k_3[O_2]}{2k_2}\left(-1 + \sqrt{1 + \frac{4k_2\overline{\Phi}e^a}{k_3k_4[H_2O][O_2]}}\right) \tag{A15}$$

Introducing Eq. (A15) into Eq. (A8), the following equation is derived:

$$[\cdot CH_2OH] = \frac{k_5[CH_3OH]}{k_6[O_2]}\frac{k_4[H_2O]}{k_5[CH_3OH] + k_7[HCHO] + k_8[\cdot OCH]} \times \frac{k_3[O_2]}{2k_2}\left(-1 + \sqrt{1 + \frac{4k_2\overline{\Phi}e^a}{k_3k_4[H_2O][O_2]}}\right) \tag{A16}$$

Introducing Eq. (A10) into Eq. (A16):

$$[\cdot CH_2OH] = \frac{k_5[CH_3OH]}{k_6[O_2]}\frac{k_4[H_2O]}{k_5[CH_3OH] + 2k_7[HCHO]} \times \frac{k_3[O_2]}{2k_2}\left(-1 + \sqrt{1 + \frac{4k_2\overline{\Phi}e^a}{k_3k_4[H_2O][O_2]}}\right) \tag{A17}$$

Finally, the rate expression for the production of HCHO takes the form:

$$r_{HCHO} = k_6[\cdot CH_2OH][O_2] - k_7[\cdot OH][HCHO] \tag{A18}$$

Assuming that under conditions of excess of methanol and presence of oxygen the formation of formaldehyde from methanol is quantitative [33], further oxidation can be neglected:

$$r_{HCHO} \approx k_6[\cdot CH_2OH][O_2] \tag{A19}$$

Introducing Eq. (A17) into (A19):

$$r_{HCHO} = k_6[O_2]\frac{k_5[CH_3OH]}{k_6[O_2]}\frac{k_4[H_2O]}{k_5[CH_3OH]+2k_7[HCHO]}\frac{k_3[O_2]}{2k_2}\left(-1 + \sqrt{1 + \frac{4k_2\overline{\Phi}e^a}{k_3k_4[H_2O][O_2]}}\right)$$

$$r_{HCHO} = \alpha_1\frac{[CH_3OH]}{[CH_3OH]+\alpha_3[HCHO]}\left(-1 + \sqrt{1 + \alpha_2 e^a}\right) \tag{A20}$$

where $\alpha_1 = \frac{k_3k_4[H_2O][O_2]}{2k_2}$, $\alpha_2 = \frac{4k_2\overline{\Phi}}{k_3k_4[H_2O][O_2]}$ and $\alpha_3 = \frac{2k_7}{k_5}$ and the concentration of water and dissolved oxygen can be considered constant.

## Limiting case

When methanol is in a large excess, $\alpha_3[HCHO] << [CH_3OH]$, Eq. (A20) will take the form:

$$r_{HCHO} = \alpha_1\left(-1 + \sqrt{1 + \alpha_2 e^a}\right) \tag{A21}$$

Moreover, for low irradiation conditions, $\alpha_2 e^a << 1$, taken the first term of the square root Taylor expansion, Eq. (A21) will take the form:

$$r_{HCHO} = \alpha e^a \tag{A22}$$

## References


[1] J. Kumar, A. Bansal, CFD simulations of immobilized-titanium dioxide based annular photocatalytic reactor: model development and experimental validation, Indian J. Chem. Technol. 22 (2015) 95–104.
[2] A. Buthiyappan, R. Abdul Aziz Abdul, A. Wan Daud Wan Mohd, Degradation performance and cost implication of UV-integrated advanced oxidation processes for wastewater treatments, Rev. Chem. Eng. 31 (3) (2015) 263–302.
[3] M.E. Leblebici, G.D. Stefanidis, T. Van Gerven, Comparison of photocatalytic space-time yields of 12 reactor designs for wastewater treatment, Chem. Eng. Process. 97 (2015) 106–111.
[4] R. Lakerveld, G. Sturm, A. Stankiewicz, G.D. Stefanidis, Integrated design of microwave and photocatalytic reactors. Where are we now?, Curr Opin. Chem. Eng. 5 (2014) 37–41.
[5] T. Van Gerven, G. Mul, J. Moulijn, A. Stankiewicz, A review of intensification of photocatalytic processes, Chem. Eng. Process. 46 (2007) 781–789.
[6] M. Subramanian, A. Kannan, Photocatalytic degradation of phenol in a rotating annular reactor, Chem. Eng. Sci. 65 (2010) 2727–2740.
[7] J. Kumar, A. Bansal, CFD modeling of hydrodynamics and mass transfer of Rhodamine B in annular reactor, Heat Mass Transfer 48 (2012) 2069–2077.
[8] J.E. Duran, F. Taghipour, M. Mohseni, CFD modeling of mass transfer in annular reactors, Int. J. Heat Mass Transfer 52 (2009) 5390–5401.
[9] D.A. Sozzi, F. Taghipour, Computational and experimental study of annular photo-reactor hydrodynamics, Int. J. Heat Fluid Flow 27 (2006) 1043–1053.
[10] F. Jović, V. Kosar, V. Tomašić, Z. Gomzi, Non-ideal flow in an annular photocatalytic reactor, Chem. Eng. Res. Des. 90 (2012) 1297–1306.
[11] D. Santoro, M. Raisee, M. Moghaddami, J. Ducoste, M. Sasges, L. Liberti, M. Notarnicola, Modeling hydroxyl radical distribution and trialkyl phosphates oxidation in UV–$H_2O_2$ photoreactors using computational fluid dynamics, Environ. Sci. Technol. 44 (2010) 6233–6241.
[12] J.E. Duran, M. Mohseni, F. Taghipour, Computational fluid dynamics modeling of immobilized photocatalytic reactors for water treatment, AIChE J. 57 (2011) 1860–1872.
[13] J.E. Duran, F. Taghipour, M. Mohseni, Irradiance modeling in annular photoreactors using the finite-volume method, J. Photochem. Photobiol. A 215 (2010) 81–89.
[14] V.K. Pareek, A.A. Adesina, Light intensity distribution in a photocatalytic reactor using finite volume, AIChE J. 50 (2004) 1273–1288.
[15] A. Queffeulou, L. Geron, C. Archambeau, H.L. Gall, P.-M. Marquaire, O. Zahraa, Kinetic study of acetaldehyde photocatalytic oxidation with a thin film of $TiO_2$ coated on stainless steel and CFD modeling approach, Ind. Eng. Chem. Res. 49 (2010) 6890–6897.
[16] G. Vincent, E. Schaer, P.-M. Marquaire, O. Zahraa, CFD modelling of an annular reactor, application to the photocatalytic degradation of acetone, Process Saf. Environ. Prot. 89 (2011) 35–40.
[17] J.E. Duran, M. Mohseni, F. Taghipour, Modeling of annular reactors with surface reaction using computational fluid dynamics (CFD), Chem. Eng. Sci. 65 (2010) 1201–1211.
[18] C. Passalia, O.M. Alfano, R.J. Brandi, A methodology for modeling photocatalytic reactors for indoor pollution control using previously estimated kinetic parameters, J. Hazard. Mater. 211 (2012) 357–365.
[19] S. Elyasi, F. Taghipour, Simulation of UV photoreactor for degradation of chemical contaminants: model development and evaluation, Environ. Sci. Technol. 44 (2010) 2056–2063.
[20] G.E. Imoberdorf, H.A. Irazoqui, O.M. Alfano, A.E. Cassano, Scaling-up from first principles of a photocatalytic reactor for air pollution remediation, Chem. Eng. Sci. 62 (2007) 793–804.
[21] M. Motegh, J. Cen, P.W. Appel, J.R. van Ommen, M.T. Kreutzer, Photocatalytic-reactor efficiencies and simplified expressions to assess their relevance in kinetic experiments, Chem. Eng. J. 207 (2012) 607–615.
[22] A. Manassero, M.L. Satuf, O.M. Alfano, Evaluation of UV and visible light activity of $TiO_2$ catalysts for water remediation, Chem. Eng. J. 225 (2013) 378–386.
[23] C. Pablos, J. Marugán, R. van Grieken, C. Adán, A. Riquelme, J. Palma, Correlation between photoelectrochemical behaviour and photoelectrocatalytic activity and scaling-up of P25-$TiO_2$ electrodes, Electrochim. Acta 130 (2014) 261–270.
[24] J.M. Erikson, H.G. Biggs, 1,4-Dihydro-3,5-diacetyl lutidine. A basis for triglyceride determination in biological samples, J. Chem. Educ. 50 (1973) 631–632.
[25] O. Levenspiel, Chemical reaction engineering, Ind. Eng. Chem. Res. 38 (1999) 4140–4143.
[26] E. Sahle-Demessie, S. Bekele, U.R. Pillai, Residence time distribution of fluids in stirred annular photoreactor, Catal. Today 88 (2003) 61–72.
[27] N. Miložič, M. Lubej, U. Novak, P. Žnidaršič-Plazl, I. Plazl, Evaluation of diffusion coefficient determination using a microfluidic device, Chem. Biochem. Eng. Q. 28 (2014) 215–223.
[28] A.E. Cassano, O.M. Alfano, Reaction engineering of suspended solid heterogeneous photocatalytic reactors, Catal. Today 58 (2000) 167–197.
[29] Y. Boyjoo, M. Ang, V. Pareek, Lamp emission and quartz sleeve modelling in slurry photocatalytic reactors, Chem. Eng. Sci. 111 (2014) 34–40.
[30] Y. Boyjoo, M. Ang, V. Pareek, Some aspects of photocatalytic reactor modeling using computational fluid dynamics, Chem. Eng. Sci. 101 (2013) 764–784.
[31] M.L. Satuf, R.J. Brandi, A.E. Cassano, O.M. Alfano, Photocatalytic degradation of 4-chlorophenol: a kinetic study, Appl. Catal., B: Environ 82 (2008) 37–49.

[32] J. Marugán, R. van Grieken, C. Pablos, M.L. Satuf, A.E. Cassano, O.M. Alfano, Rigorous kinetic modelling with explicit radiation absorption effects of the photocatalytic inactivation of bacteria in water using suspended titanium dioxide, Appl. Catal., B: Environ. 102 (2011) 404–416.
[33] L. Sun, J.R. Bolton, Determination of the quantum yield for the photochemical generation of hydroxyl radicals in $TiO_2$ suspensions, J. Phys. Chem. 100 (10) (1996) 4127–4134.
[34] C. Wang, J. Rabani, D.W. Bahnemann, J.K. Dohrmann, Photonic efficiency and quantum yield of formaldehyde formation from methanol in the presence of various $TiO_2$ photocatalysts, J. Photochem. Photobiol. A: Chem. 148 (2002) 169–176.
[35] Jian-Jun Yang, Dong-Xu Li, Qing-Lin Li, Zhi-Jun Zhang, Han-Qing Wang, Mechanism of photocatalytic oxidation of formaldehyde, Acta Phys. Chim. Sin. 17 (3) (2001) 278–281.
[36] J. Marugán, R. van Grieken, C. Pablos, M.L. Satuf, A.E. Cassano, O.M. Alfano, Modeling of a bench-scale photocatalytic reactor for water disinfection from laboratory-scale kinetic data, Chem. Eng. J. 224 (2013) 39–45.
[37] J. Colina-Marquez, F. Machuca-Martínez, G. Li-Puma, Radiation absorption and optimization of solar photocatalytic reactors for environmental applications, Environ. Sci. Technol. 44 (2010) 5112–5120.